

# *Gyrokinetic particle simulation of microturbulence for general magnetic geometry and experimental profiles*

Y. Xiao<sup>1,2</sup>, Ihor Holod<sup>2</sup>, Zhixuan Wang<sup>2</sup>, Zhihong Lin<sup>2,3</sup>, Taige Zhang<sup>1</sup>

<sup>1</sup>Institute for Fusion Theory and Simulation, Zhejiang University, Hangzhou, 310027, China

<sup>2</sup>Department of Physics and Astronomy, University of California, Irvine, CA 92697, U.S.A

<sup>3</sup>Fusion Simulation Center, Peking University, Beijing, 100871, China

Date: 10/06/2013

**Abstract.** New developments in the gyrokinetic particle simulation enable the GTC code to simulate turbulent transport in tokamaks with realistic equilibrium profiles and plasma geometry, which is a critical step in the code-experiment validation process. These new developments include numerical equilibrium representation using B-spline, a new Poisson solver based on finite difference using field-aligned mesh and magnetic flux coordinates, a new zonal flow solver under general geometry, improvements on the conventional four-point gyroaverage, nonuniform background marker loading. With these new futures GTC is able to simulate a typical DIII-D discharge with experimental magnetic geometry and profiles. The simulated turbulent heat diffusivity and its radial profile show good agreement with other gyrokinetic code. The newly-developed nonuniform loading method gives a different radial transport profile from the conventional uniform loading and the underlying physics is explained.

## *I. Introduction*

A complete understanding of the physics of anomalous transport is critical for designing future magnetic fusion reactors [1]. It is generally believed that the turbulence in ion gyroradius scale (micro-scale) leads to the anomalous transport [2] observed in experiments. For low beta and high temperature toroidal plasmas, electrostatic modes may contribute most to the turbulent transport. The ion temperature gradient (ITG) mode [2, 3] and collisionless trapped electron mode (CTEM) [4] are two prominent candidates accounting for ion and electron turbulent transport respectively. By several decades' development, massively parallel gyrokinetic simulation based on first-principles has emerged as a major tool to investigate the complicated physics of the turbulent transport [5].

The code development for these large scale gyrokinetic simulations has experienced several stages. In the beginning, the code is implemented based on the gyrokinetic model and then verified by some analytic theory and other numerical codes to assure that the code faithfully represented the simulation model [6, 7]. The next step is to use the existing code to carry out various interesting but complicated physics studies such as saturation mechanism and transport mechanism of the turbulence [8, 9]. The third step is called code validation [10-12], which is usually parallel to the aforementioned second stage. In this step the gyrokinetic simulation is performed using the real experiment parameters. The simulation results, such as the transport flux, temporal and spatial characteristics of the turbulence, are compared to the experimental measurements to help explain experiments and in the other hand, to verify that the simulation model has captured the essential physics of the turbulent transport. After all the comprehensive comparison between code, simulation model and experiments, the code is expected to have a predictive power. The ultimate goal of the gyrokinetic code development is applied to guide new campaign of experiments and help design next generation of tokamaks.

The current efforts on the gyrokinetic code development still focus on the first three stages. Especially, the code validation step is a critical step in this roadmap. The main purpose of this article is to report the recent progress of the global gyrokinetic particle code (GTC) [5, 13], on incorporating general equilibrium magnetic geometry and real experimental profiles to simulate the turbulent transport in tokamak experiments. In fact, these new features developed in this work have already been used successfully to validate GTC simulations of Alfvén eigenmodes [14, 15] in DIII-D experiments and to study the trapped electron mode (TEM) instability in the pedestal of DIII-D H-mode plasmas [16]. The general geometry capability can also be readily utilized together with the recent upgrades of GTC physics models for global simulations of macroscopic MHD instabilities excited by equilibrium current [17] and radio frequency waves in tokamaks [18].

In this work, we develop a numerical scheme based on B-splines to calculate the equilibrium quantities on the computational mesh grids or evaluate the field quantities at the particle position. This new feature enables the usage of numerical magnetic equilibrium produced by MHD equilibrium codes such as EFIT[19, 20], VMEC[21] and TRANSP[21, 22]. In order to accommodate the general magnetic geometry, we make improvements on the conventional four point average method [23] to calculate gyroaverage, and we also implement a new gyrokinetic Poisson solver based on the Pade approximation. Since the field-aligned magnetic coordinates are employed, this new Poisson solver in the GTC code is able to simulate small aspect ratio tokamaks such as NSTX in addition to the conventional large aspect ratio tokamaks. A new zonal flow solver is developed for the general magnetic geometry. We also implement a nonuniform loading method for the background marker

distribution in addition to the conventional uniform loading method. Next we use DIII-D discharge #101391 as a benchmark case for these new developments in the GTC code. In the simulation, we include kinetic electrons and find this discharge is an ITG-mode-dominating case. We compare the heat diffusivity for different gyrokinetic Poisson solvers and different marker loading methods. The new gyrokinetic Poisson solver gives about the same turbulent transport level as the conventional four-point average method. In addition, the nonuniform loading method gives about the same volume averaged turbulent transport as the conventional uniform loading. However, the radial profile of the turbulent transport is different for these two loading methods, which can be understood by the stabilizing effect of the gyroaverage, i.e., the finite Larmor radius (FLR) effect. The simulation results are compared to that from GYRO [24, 25] and good agreement is obtained.

The remainder of this paper is organized as follows. In Section II, we provide an introduction to numerical representation of equilibrium plasma quantities, especially the B-spline interpolation. In Section III, the  $\delta f$  method to solve gyrokinetic equation and particle pushing scheme in general magnetic geometry are reviewed for completeness. Then we explained how to use the Pade approximation to solve gyrokinetic Poisson equation and the associated zonal flow component in Section IV, where the conventional 4-point average method is also improved. The finite difference scheme is used to discretize the Laplacian operator and then is verified by examples, as shown in Section V. Based on the preceding improvements, a gyrokinetic turbulence simulation is carried out and benchmarked with DIII-D experimental parameters in Section VI. Summary and discussion are provided in Section VII.

## ***II. Numerical representation of equilibrium plasma quantities***

In the plasma turbulence studies we often divide physical quantities into an equilibrium part and a fluctuating part. The equilibrium quantities obey the MHD equilibrium, i.e., the Grad-Shafranov equation, while the fluctuating part is driven by various instabilities that lead to turbulent transport. The equilibrium magnetic configuration used by the gyrokinetic simulation are either from analytic models, such as simple circular cross section or Miller equilibrium, or from other numeric equilibrium codes, such as EFIT[19, 20] or TRANSP[21, 22]. The equilibrium in tokamaks can be better described by the magnetic flux coordinates instead of the Cartesian coordinates, because some important equilibrium quantities, such as plasma temperature and density, can be shown to depends on the magnetic flux only. The GTC code employs magnetic flux coordinates  $(\psi, \theta, \zeta)$  to represent the electromagnetic fields and plasma profiles, where  $\psi$  is the poloidal magnetic flux,  $\theta$  is the poloidal

angle and  $\zeta$  is the toroidal angle. The equilibrium magnetic field can be represented either in the following covariant form

$$\mathbf{B}_0 = g\nabla\zeta + I\nabla\theta + \delta\nabla\psi, \quad (1)$$

or in the contravariant form

$$\mathbf{B}_0 = q\nabla\psi \times \nabla\theta + \nabla\zeta \times \nabla\psi. \quad (2)$$

Then the transformation Jacobian takes the following form

$$J^{-1} \equiv \nabla\psi \times \nabla\theta \cdot \nabla\zeta = \frac{B_0^2}{gq + I}. \quad (3)$$

If the Jacobian is properly chosen such that  $(\psi, \theta, \zeta)$  are the Boozer coordinates, the toroidal current  $g$  and poloidal current  $I$ , can be represented by a sole function of  $\psi$ , i.e.,  $g = g(\psi)$ ,  $I = I(\psi)$ .

The GTC code inputs the numerical magnetic equilibrium and plasma profiles from EFIT/TRANSP by transforming the equilibrium quantities defined in the toroidal coordinates  $(R, Z, \phi)$  to those defined in the magnetic coordinates  $(\psi, \theta, \zeta)$ . However, the EFIT outputs only provide equilibrium quantities on a coarse mesh, which usually contains a few tens of grid points in the radial or poloidal direction. This is insufficient to simulate ion gyroradius ( $\rho_i$ ) scale microturbulence, which requires hundreds to thousands of grid points in the radial and poloidal direction for the size of a realistic tokamak. Therefore, it is necessary to map the coarse experimental mesh to the fine computational mesh to achieve sufficient numerical accuracy.

The B-splines, which are first order continuous, are currently implemented in the GTC code for the 1D and 2D functions to interpolate the complicated magnetic geometry and plasma profiles, which provides a good compromise between high numerical confidence and reasonable computation efficiency. Generally two classes of functions are involved in the representing magnetic geometry and plasma profiles, one dimensional function  $f(\psi)$  or two dimensional function  $f(\psi, \theta)$ . For the 1D function  $f(\psi)$ , such as ion temperature profile  $T_i(\psi)$  and toroidal current  $g(\psi)$ , we can use the following B-spline representation

$$f(\psi) = f(1, i) + f(2, i)h + f(3, i)h^2, \quad (4)$$

where  $\psi_i \leq \psi < \psi_{i+1}$ ,  $h = \psi_{i+1} - \psi_i$ ,  $i = 0, 1, \dots, N$ , and  $f(1, i) = f(\psi_i)$ . Here we assume uniform grid size in the radial direction. The coefficients  $f(2, i)$  and  $f(3, i)$  can be calculated from  $f(1, i)$ , as discussed in Appendix I.

After constructing 1D B-splines, the derivative of the spline function can easily be found as

$$f'(\psi_i) = f(2, i) + 2hf(3, i) \quad (5)$$

This expression is useful to evaluate the temperature gradient,  $dT(\psi)/d\psi$ , and density gradient,  $dn(\psi)/d\psi$ , which are the main instability drives for the microturbulences.

With these 1-D spline functions constructed, we can proceed to construct B-spline functions for one class of very useful 2D functions  $f(\psi, \theta) = \sum_n g_n(\psi)h_n(\theta)$ , which can be used to describe most tokamak equilibrium magnetic configurations. Each function  $g_n(\psi)$  or  $h_n(\theta)$  can be represented by the 1D B-splines, i.e.,  $g_n(\psi) = g_n(i, 1) + g_n(i, 2)\Delta\psi + g_n(i, 3)\Delta\psi^2$  and  $h_n(\theta) = h_n(i, 1) + h_n(i, 2)\Delta\theta + h_n(i, 3)\Delta\theta^2$ . Then the 2D function  $f(\psi, \theta)$  can be expressed by the following equation to the accuracy of the second order.

$$\begin{aligned} f(\psi, \theta) = & f(1, i, j) + f(2, i, j)\Delta\psi + f(3, i, j)\Delta\psi^2 \\ & + f(4, i, j)\Delta\theta + f(5, i, j)\Delta\psi\Delta\theta + f(6, i, j)\Delta\theta\Delta\psi^2 \\ & + f(7, i, j)\Delta\theta^2 + f(8, i, j)\Delta\psi\Delta\theta^2 + f(9, i, j)\Delta\psi^2\Delta\theta^2, \end{aligned} \quad (6)$$

where the coefficients  $f(m, i, j)$ ,  $m = 1, \dots, 9$ , can be related by the spline coefficients  $g_n(i, l)$  and  $h_n(i, l)$ . The derivatives of  $f(\psi, \theta)$  on the grid points, to the accuracy of first order, can be found as

$$\begin{aligned} f_\psi(\psi, \theta) = & f(2, i, j) + f(5, i, j)\Delta\theta + f(8, i, j)\Delta\theta^2 \\ & + 2\Delta\psi[f(3, i, j) + f(6, i, j)\Delta\theta + f(9, i, j)\Delta\theta^2], \end{aligned} \quad (7)$$

$$\begin{aligned} f_\theta(\psi, \theta) = & f(4, i, j) + f(5, i, j)\Delta\psi + f(6, i, j)\Delta\psi^2 \\ & + 2\Delta\theta[f(7, i, j) + f(8, i, j)\Delta\psi + f(9, i, j)\Delta\psi^2]. \end{aligned} \quad (8)$$

These expressions are particularly useful for calculating the relevant physical quantities, such as

$\partial B/\partial \psi$  and  $\partial B/\partial \theta$ , which will be used to compute the particle motion in the gyrokinetic simulation.

### III. Gyrokinetic equation and particle pushing in general geometry

Gyrokinetic particle simulation uses the particle-in-cell method to solve gyrokinetic equation, which is essentially a Monte-Carlo approach to solve the reduced dynamic equation in the 5D phase space of  $(\psi, \zeta, \theta, v_{\parallel}, \mu)$ , where  $\mu = m v_{\perp}^2/2B$  is the magnetic moment and  $v_{\parallel}$  is the parallel velocity for the particle. In the simulation a large number of particles are initiated to satisfy the equilibrium distribution and then evolve according to equations of motion in the 5D phase space. After these particles are relocated, the electromagnetic fields are computed by Gyrokinetic Poisson equation through gathering the charges on the mesh grids and hence the particles can be pushed to the next time step. In order to minimize the Monte-Carlo noise caused by the particle method, the  $\delta f$  algorithm is usually applied in the gyrokinetic simulation, which separate the perturbed distribution function  $\delta f$  from the total particle distribution  $f = \delta f + F_M$ . The equilibrium distribution  $F_M$  is noiseless in this algorithm and the  $\delta f$  algorithm can improve the noise to signal ratio by a factor of  $F_M/\delta f$ .

In the GTC code, we apply gyrokinetics for ions and drift kinetics for electrons since we focus on the turbulence on the ion gyroradius scale. The ion distribution function  $f_i = f_{Mi} + \delta f_i$ , with the perturbed guiding center distribution function  $\delta f_i$  satisfying the following gyrokinetic equation [26]

$$\begin{aligned} \frac{d\delta f_i}{dt} &\equiv \left[ \frac{\partial}{\partial t} + (v_{\parallel} \mathbf{b} + \mathbf{v}_d + \langle \mathbf{v}_E \rangle_{\varphi}) \cdot \nabla - \mathbf{b}^* \cdot \nabla (\mu B + Z_i e \langle \phi \rangle_{\varphi}) \frac{\partial}{m_i \partial v_{\parallel}} \right] \delta f_i \\ &= -f_{Mi} \left( \langle \mathbf{v}_E \rangle_{\varphi} \cdot \nabla \ln f_{Mi} + \mathbf{b}^* \cdot \nabla \langle \phi \rangle_{\varphi} \frac{Z_i e \partial}{m_i \partial v_{\parallel}} \ln f_{Mi} \right) \end{aligned} \quad (9)$$

In this equation,  $\mathbf{b}^* = \mathbf{b} + \frac{m_i c}{Z_i e B} v_{\parallel} \nabla \times \mathbf{b}$ ,  $\mu = \frac{m_i v_{\perp}^2}{2B}$ ,  $\langle \mathbf{v}_E \rangle_{\varphi} = \frac{c \mathbf{b} \times \nabla \langle \phi \rangle_{\varphi}}{B}$  with

$\langle \phi \rangle_{\varphi} = \frac{1}{2\pi} \int \phi(\mathbf{x}) \delta(\mathbf{x} - \mathbf{R} - \boldsymbol{\rho}) d\mathbf{x} d\varphi$  the gyroaveraged electrostatic potential,  $\mathbf{v}_d = \mathbf{v}_c + \mathbf{v}_g$  with

$\mathbf{v}_c = \frac{v_{\parallel}^2}{\Omega_i} \nabla \times \mathbf{b}$  and  $\mathbf{v}_g = \frac{\mu}{m_i \Omega_i} \mathbf{b} \times \nabla B$ . Decompose the electrostatic potential to a flux-surface

averaged component (zonal component) and a fluctuating component, i.e.,  $\phi = \langle \phi \rangle + \delta \phi$  with  $\langle \delta \phi \rangle = 0$ .

The electrons may mostly respond to the fluctuating potential adiabatically due to the fast electron motion. Therefore, it is convenient to write the electron distribution function

as  $f_e = f_{Me} + \frac{e\delta\phi}{T_e} f_{Me} + \delta g_e$ , with  $\frac{e\delta\phi}{T_e} \ll 1$  and  $\delta g_e$  satisfying the following drift kinetic equation [27]

$$\begin{aligned} & \left[ \frac{\partial}{\partial t} + (v_{\parallel} \mathbf{b} + \mathbf{v}_d + \mathbf{v}_E) \cdot \nabla - \mathbf{b}^* \cdot \nabla (\mu B - e\phi) \frac{\partial}{m_e \partial v_{\parallel}} \right] \delta g_e \\ & = -f_{Me} \exp\left(\frac{e\delta\phi}{T_e}\right) \left( \frac{\partial}{\partial t} \left( \frac{e\delta\phi^{(0)}}{T_e} \right) + \delta \mathbf{v}_E \cdot \nabla \ln f_{Me} - (\mathbf{v}_d + \delta \mathbf{v}_E) \cdot \nabla \left( \frac{e\langle \phi \rangle}{T_e} \right) \right), \end{aligned} \quad (10)$$

where  $\delta \mathbf{v}_E = \frac{c \mathbf{b} \times \nabla \langle \delta \phi \rangle_{\varphi}}{B}$ .

In the  $\delta f$  algorithm, the particle weight  $w = \delta f / f$  works as an additional attribute to the particles. The evolution of the particle weight is determined by the following equation [28]

$$\frac{dw}{dt} = \frac{1-w}{F_M} \frac{d\delta f}{dt} \quad (11)$$

The original equation of motion in the Boozer coordinates [29] can be applied without modification to the general magnetic geometry case. For completeness, we list the equation of motion implemented in GTC for the electrostatic simulation:

$$\dot{\zeta} = \frac{\bar{\rho}_{\parallel} \bar{B}^2}{\bar{D}} (q + \bar{\rho}_{\parallel} \bar{I}') - \frac{1}{Z_{\alpha}} \left( \bar{\mu} + \frac{Z_{\alpha}^2}{m_{\alpha}} \bar{\rho}_{\parallel}^2 \bar{B} \right) \frac{\bar{I}}{\bar{D}} \frac{\partial \bar{B}}{\partial \bar{\psi}} - \frac{\bar{I}}{\bar{D}} \frac{\partial \bar{\phi}}{\partial \bar{\psi}} \quad (12)$$

$$\dot{\theta} = \frac{\bar{\rho}_{\parallel} \bar{B}^2}{\bar{D}} (1 - \bar{\rho}_{\parallel} \bar{g}') + \frac{1}{Z_{\alpha}} \left( \bar{\mu} + \frac{Z_{\alpha}^2}{m_{\alpha}} \bar{\rho}_{\parallel}^2 \bar{B} \right) \frac{\bar{g}}{\bar{D}} \frac{\partial \bar{B}}{\partial \bar{\psi}} + \frac{\bar{g}}{\bar{D}} \frac{\partial \bar{\phi}}{\partial \bar{\psi}} \quad (13)$$

$$\dot{\bar{\psi}} = -\frac{1}{Z_{\alpha}} \frac{\bar{g}}{\bar{D}} \left( \bar{\mu} + \frac{Z_{\alpha}^2}{m_{\alpha}} \bar{\rho}_{\parallel}^2 \bar{B} \right) \frac{\partial \bar{B}}{\partial \theta} + \frac{1}{Z_{\alpha}} \frac{\bar{I}}{\bar{D}} \left( \bar{\mu} + \frac{Z_{\alpha}^2}{m_{\alpha}} \bar{\rho}_{\parallel}^2 \bar{B} \right) \frac{\partial \bar{B}}{\partial \zeta} + \frac{\bar{I}}{\bar{D}} \frac{\partial \bar{\phi}}{\partial \zeta} - \frac{\bar{g}}{\bar{D}} \frac{\partial \bar{\phi}}{\partial \bar{\psi}} \quad (14)$$

$$\begin{aligned} \dot{\bar{\rho}}_{\parallel} = & \frac{1}{Z_{\alpha}} \frac{(1 - \bar{\rho}_{\parallel} \bar{g}') \left( \bar{\mu} + \frac{Z_{\alpha}^2}{\bar{m}_{\alpha}} \bar{\rho}_{\parallel}^2 \bar{B} \right)}{\bar{D}} \frac{\partial \bar{B}}{\partial \theta} - \frac{(1 - \bar{\rho}_{\parallel} \bar{g}')}{\bar{D}} \frac{\partial \bar{\phi}}{\partial \theta} \\ & - \frac{(\bar{q} + \bar{\rho}_{\parallel} \bar{I}')}{\bar{D}} \frac{\partial \bar{\phi}}{\partial \zeta} - \frac{1}{Z_{\alpha}} \frac{(q + \bar{\rho}_{\parallel} \bar{I}') \left( \bar{\mu} + \frac{Z_{\alpha}^2}{\bar{m}_{\alpha}} \bar{\rho}_{\parallel}^2 \bar{B} \right)}{\bar{D}} \frac{\partial \bar{B}}{\partial \zeta} \end{aligned} \quad (15)$$

This set of equations is based on a Hamiltonian principle, with the Hamiltonian  $H = \bar{\rho}_{\parallel}^2 \bar{B}^2 / 2 + \bar{\mu} \bar{B} + \bar{\phi}$ , which is suitable for determining the motion of the guiding centers of both ions and electrons. The physical quantities in the preceding equations are all normalized quantities:

$$\bar{\psi} = \frac{\psi}{B_0 R_0^2}, \bar{\rho}_{\parallel} = \frac{\bar{v}_{\parallel}}{\Omega_{\alpha}} = \frac{v_{\parallel}}{R_0 \Omega_{\alpha}}, \quad \bar{D} = \frac{1}{B_0 R_0} (qg + I + \bar{\rho}_{\parallel} (gI' - Ig')) \quad , \quad \bar{I} = \frac{I}{B_0 R_0}, \bar{I}' = \frac{d\bar{I}}{d\bar{\psi}} \quad ,$$

$$\bar{g} = \frac{g}{B_0 R_0}, \bar{g}' = \frac{dg}{d\bar{\psi}}, \bar{m}_{\alpha} = \frac{m_{\alpha}}{m_H}, \bar{\phi} = \frac{e \langle \phi \rangle_{\phi}}{m_H R_0^2 \Omega_0^2} \quad , \quad \text{with } m_H \text{ hydrogen mass, } \Omega_0 = \frac{e B_0}{m_H c} \text{ hydrogen}$$

gyrofrequency,  $R_0$  tokamak major radius and  $B_0$  the magnetic field at magnetic axis. However, we

note in Ref. [29] this set of equations are normalized by the particle gyrofrequency  $\Omega_{\alpha} = \frac{Z_{\alpha} e B_0}{m_{\alpha} c}$ .

With some minor modifications, these equations of motion can also be used to push particle in the presence of electromagnetic perturbations [13, 29].

#### IV. Poisson solver in the general magnetic geometry

To close the preceding gyrokinetic equations, we need to use the following gyrokinetic Poisson equation:

$$\frac{Z_i^2 e n_{0i}}{T_i} (\phi - \tilde{\phi}) = Z_i \bar{n}_{i1} - n_{e1} \quad (16)$$

with  $\tilde{\phi} = \frac{1}{2\pi} \int \langle \phi \rangle_{\phi}(\mathbf{R}) \delta(\mathbf{x} - \mathbf{R} - \rho) F_{Mi}(\mathbf{R}, \mu, v_{\parallel}) d\mathbf{R} d\mu dv_{\parallel} d\phi$  [30]. The electron may be dominated by adiabatic response due to the fast electron motion in the ambient turbulence. Therefore, it is convenient to write  $n_{e1} = (1 - \delta_m) n_{e0} e \phi / T_e + \delta n_e^{(1)}$ , with  $\delta_m = 0$  for electrostatic case and  $\delta_m = 1$  for electromagnetic case. So we obtain the following gyrokinetic poisson equation [13, 27, 31]:

$$\left( \frac{Z_i^2 en_{i0}}{T_i} + \frac{en_{e0}}{T_e} \delta_m \right) \phi - \frac{Z_i^2 en_{i0}}{T_i} \tilde{\phi} = Z_i \bar{n}_{i1} - \delta n_e^{(1)} \quad (17)$$

There are two approaches to evaluate  $\tilde{\phi}$ , the 4-point average or Pade approximation. The 4-point average method is illustrated in Ref. [32] which is shown in Fig. 3(a). However, the 4-point method conventionally implemented in GTC is only accurate in the local approximation when  $r \gg \rho_i$ , since it only retains the leading order term in the  $\rho_i/r$  expansion. This conventional method is shown by the dark red points in Fig. 3(b). In order to capture the global effects, the traditional method needs to retain higher order terms, e.g., the first order correction, as shown by the fresh red points in Fig. 3(b).

We note that in long wave length limit  $\tilde{\phi} \approx -\rho_i^2 \nabla_{\perp}^2 \phi$ . Hence one crucial step to verify the improved 4-point average method for the gyrokinetic Poisson equation is to show that it can be used to solve the Poisson problem  $-\nabla_{\perp}^2 \phi = \delta n$ . In the high q limit, the toroidal effects can be ignored. Considering a circular cross section tokamak, the Laplacian operator can be approximated as

$\nabla_{\perp}^2 = \frac{1}{r} \frac{\partial}{\partial r} r \frac{\partial}{\partial r} + \frac{1}{r^2} \frac{\partial^2}{\partial \theta^2}$ . This Poisson problem essentially becomes a Bessel problem. Then if we

let  $\delta n(r, \theta) = J_0(k_0 r) - \frac{J_0(k_0 a_1)}{Y_0(k_0 a_1)} Y_0(k_0 r)$ , with  $k_0$  satisfying  $J_0(k_0 a_0) Y_0(k_0 a_1) - J_0(k_0 a_1) Y_0(k_0 a_0) = 0$ ,

the Poisson equation has a theory solution  $\phi = J_0(k_0 r) - \frac{J_0(k_0 a_1)}{Y_0(k_0 a_1)} Y_0(k_0 r)$ , under the boundary

condition  $\phi(r = a_0) = \phi(r = a_1) = 0$ . As shown by Fig. 6, the solid lines shows the theory solution, while the lines with different shapes show the different number of radial grids applied in the numeric calculation. Fig. 4(a) shows the solutions from the conventional local approximation for the 4-point average method for different numbers of radial grids, while Fig. 4(b) shows the solution by adding higher order global corrections to 4-point average method. As one can see from these figures, the new implementation of the global correction makes the numeric solution more close to the theory value.

Next we discuss the second method to evaluate  $\tilde{\phi}$ , the Pade approximation, as demonstrated as following.

$$\tilde{\phi} = \frac{-\rho_i^2 \nabla_{\perp}^2}{1 - \rho_i^2 \nabla_{\perp}^2} \phi \quad (18)$$

Decompose the electrostatic potential and density perturbation to a flux-surface averaged component (zonal component) and a fluctuating component, i.e.,  $\phi = \langle \phi \rangle + \delta\phi, n_1 = \langle n_1 \rangle + \delta n$ , with  $\langle \delta n \rangle = \langle \delta\phi \rangle = 0$ . The flux-surface average is calculated by  $\langle \phi \rangle \equiv \frac{\int d\theta d\zeta J \phi}{\int d\theta d\zeta J}$ . Subtracting Eq.(16) by its flux-surface average gives

$$\delta\phi - \tilde{\delta\phi} + \langle \tilde{\phi} \rangle - \langle \phi \rangle = \frac{T_i e}{n_i Z_i^2} (Z_i \delta \bar{n}_i - \delta n_e) \quad (19)$$

In the large aspect ratio limit, the term  $\langle \tilde{\phi} \rangle - \langle \phi \rangle$  in the preceding equation mainly represents the coupling between equilibrium magnetic field and  $\phi_{n=0, m \neq 0}$  harmonics, which is transparent in the long wavelength limit  $\langle \tilde{\phi} \rangle - \langle \phi \rangle = \left( k_r^2 \rho_i^2 - \langle k_r^2 \rho_i^2 \rangle \right) \langle \phi \rangle - \langle k_\perp^2 \rho_i^2 \delta\phi \rangle \approx -\langle k_\perp^2 \rho_i^2 \delta\phi \rangle$ . If we assume the equilibrium magnetic field takes the form  $B = \sum_{m=0}^{\infty} (A_m \varepsilon^m \cos^m \theta + B_m \varepsilon^m \sin^m \theta)$ , with  $\varepsilon = r/R_0$

the inverse aspect ratio, then it can be estimated  $\left( \langle \tilde{\phi} \rangle - \langle \phi \rangle \right)_{n=0, m \neq 0} \sim \varepsilon^m \delta\phi_{n=0, m \neq 0}$ , which is usually

much smaller than  $\left( \delta\phi - \tilde{\delta\phi} \right)_{n=0, m \neq 0}$  for tokamaks. Therefore, the following gyrokinetic poisson

equation can be used to compute the fluctuating potential in the requisite accuracy:

$$\delta\phi - \tilde{\delta\phi} = \frac{T_i e}{n_i Z_i^2} (Z_i \delta \bar{n}_i - \delta n_e) \quad (20)$$

The flux-surface averaged gyrokinetic Poisson equation by using Eq. (16) and (18) can be written as

$$\langle \nabla_\perp^2 \phi \rangle = \left\langle \left( \frac{T_i}{\rho_i^2 n_i Z_i^2} - \frac{T_i}{n_i Z_i^2} \nabla_\perp^2 \right) e (n_{e1} - Z_i \bar{n}_{i1}) \right\rangle \quad (21)$$

Using Eq. (25), the flux-surface averaged perpendicular Laplacian  $\langle \nabla_\perp^2 \phi \rangle$  in the preceding equation can be evaluated by

$$\langle \nabla_{\perp}^2 \phi \rangle = \frac{1}{J_0(\psi)} \left[ \frac{\partial}{\partial \psi} \left( J_0(\psi) \langle g^{\psi\psi} \rangle \frac{\partial \langle \phi \rangle}{\partial \psi} \right) + \frac{\partial J_0(\psi)}{\partial \psi} \langle g^{\psi\psi} \rangle \frac{\partial \delta \phi}{\partial \psi} + \frac{\partial J_0(\psi)}{\partial \psi} \langle g^{\psi\theta} \rangle \frac{\partial \delta \phi}{\partial \theta} \right], \quad (22)$$

Where  $J_0(\psi) = \int d\theta d\zeta J$  is the flux-surface averaged Jacobian. The ratio between the second the first term is  $\delta \phi_{m=1} / \langle \phi \rangle \ll 1$  and negligible in the large aspect ratio limit. The third term is even smaller than the second one by the factor  $g^{\psi\theta} / g^{\psi\psi}$ , where  $g^{\psi\theta}$  measures the non-orthogonality of the magnetic coordinates  $(\psi, \theta)$  and it may be small for most flux surfaces in the tokamak. Therefore, we only keep the first term in the right hand side of Eq. (22). Let  $\rho_c = e(Z_i \bar{n}_{i1} - n_{e1})$ , the gyrokinetic Poisson equation for the zonal potential  $\langle \phi \rangle$  reads as following

$$\frac{\partial}{\partial \psi} \left( J(\psi) \langle g^{\psi\psi} \rangle \frac{\partial \langle \phi \rangle}{\partial \psi} \right) = \left( -\frac{T_i}{n_i Z_i^2} J(\psi) \left\langle \frac{1}{\rho_i^2} \right\rangle + \frac{T_i}{n_i Z_i^2} \frac{\partial}{\partial \psi} J(\psi) \langle g^{\psi\psi} \rangle \frac{\partial}{\partial \psi} \right) \langle \rho_c \rangle \quad (23)$$

Integrate the preceding equation to obtain the zonal electric field

$$\frac{\partial \langle \phi \rangle}{\partial \psi} = -\frac{T_i}{n_i Z_i^2} \frac{\partial \langle \rho_c \rangle}{\partial \psi} - \frac{1}{J(\psi) \langle g^{\psi\psi} \rangle} \int_{\psi_0}^{\psi} d\psi' \frac{T_i J(\psi')}{n_i Z_i^2} \left( \left\langle \frac{1}{\rho_i^2} \right\rangle + \langle g^{\psi\psi} \rangle \frac{d \ln(T_i/n_i)}{d\psi} \frac{\partial}{\partial \psi} \right) \langle \rho_c \rangle \quad (24)$$

The preceding equation has been used in GTC to calculate the zonal flow response for a given density perturbation, which has recently reproduced the Rosenbluth-Hinton residual level [33].

## V. Laplacian operator and geometric tensor

The inversion of the Laplacian operator plays a crucial role in computing perturbed electromagnetic fields. In this section, we study how to discretize the Laplacian operator in the magnetic coordinates by the finite difference method. In the magnetic coordinate system, the Laplacian can be expressed as,

$$\nabla^2 f = \frac{1}{J} \frac{\partial}{\partial \xi^\alpha} \left( J \nabla_{\xi^\alpha} \cdot \nabla_{\xi^\beta} \frac{\partial}{\partial \xi^\beta} f \right), \text{ with } \alpha = 1, 2, 3, \text{ and } \beta = 1, 2, 3 \quad (25)$$

where  $(\xi^1, \xi^2, \xi^3) = (\psi, \theta, \zeta)$  are coordinates the jacobian  $J = (\nabla \psi \cdot \nabla \theta \times \nabla \zeta)^{-1}$ . Define a

contravariant geometric tensor  $g^{\xi^\alpha \xi^\beta} \equiv \nabla_{\xi^\alpha} \cdot \nabla_{\xi^\beta}$ . For an axisymmetric system, the Laplacian can be explicitly expressed as

$$\begin{aligned} \nabla^2 f &= g^{\psi\psi} \frac{\partial^2 f}{\partial \psi^2} + 2g^{\psi\theta} \frac{\partial^2 f}{\partial \psi \partial \theta} + g^{\theta\theta} \frac{\partial^2 f}{\partial \theta^2} + g^{\zeta\zeta} \frac{\partial^2 f}{\partial \zeta^2} \\ &+ \frac{1}{J} \left( \frac{\partial J g^{\psi\psi}}{\partial \psi} + \frac{\partial J g^{\psi\theta}}{\partial \theta} \right) \frac{\partial f}{\partial \psi} + \frac{1}{J} \left( \frac{\partial J g^{\psi\theta}}{\partial \psi} + \frac{\partial J g^{\theta\theta}}{\partial \theta} \right) \frac{\partial f}{\partial \theta} \end{aligned} \quad (26)$$

In order to compute the above Laplacian, we first need to compute the contravariant geometric tensor  $g^{\xi^a \xi^b}$ . The B-spline representation of the magnetic field provides a transformation between two coordinate systems, i.e.,  $X = X(\psi, \theta)$  and  $Z = Z(\psi, \theta)$ , where  $(X, Z, \zeta)$  are the toroidal coordinates.

The covariant geometric tensor  $g_{\xi^a \xi^b}$  can be obtained by the following formula

$$g_{\psi\psi} = \left( \frac{\partial X}{\partial \psi} \right)^2 + \left( \frac{\partial Z}{\partial \psi} \right)^2, \quad (27)$$

$$g_{\theta\theta} = \left( \frac{\partial X}{\partial \theta} \right)^2 + \left( \frac{\partial Z}{\partial \theta} \right)^2, \quad (28)$$

$$g_{\psi\theta} = \frac{\partial X}{\partial \psi} \frac{\partial X}{\partial \theta} + \frac{\partial Z}{\partial \psi} \frac{\partial Z}{\partial \theta}, \quad (29)$$

and  $g_{\theta\psi} = g_{\psi\theta}$ ,  $g_{\zeta\zeta} = X^2$ . Using the identity  $g_{\xi^a \xi^b} g^{\xi^b \xi^c} = \delta_a^c$ , we can find the transformation from the covariant to contravariant geometric tensor

$$\begin{bmatrix} g^{\psi\psi} & g^{\psi\theta} & 0 \\ g^{\theta\psi} & g^{\theta\theta} & 0 \\ 0 & 0 & g^{\zeta\zeta} \end{bmatrix} = \begin{bmatrix} g_{\theta\theta} & -g_{\psi\theta} & 0 \\ -g_{\theta\psi} & g_{\psi\psi} & 0 \\ 0 & 0 & \Delta/g_{\zeta\zeta} \end{bmatrix} \frac{1}{\Delta}, \quad (30)$$

with the determinant  $\Delta = g_{\psi\psi} g_{\theta\theta} - g_{\psi\theta} g_{\theta\psi}$ .

Closely related to the magnetic coordinates, the field aligned coordinates  $(\psi, \theta_0, \zeta_0)$  is employed in the GTC code to define field-aligned mesh, which is essential to reduce the number of toroidal grids, where  $\theta_0 = \theta - \zeta/q$  and  $\zeta_0 = \zeta$ . Then the Laplacian in this new coordinate system becomes

$$\begin{aligned} \nabla^2 f &= g^{\psi\psi} \frac{\partial^2 f}{\partial \psi^2} + 2g^{\psi\theta} \frac{\partial^2 f}{\partial \psi \partial \theta_0} + g^{\theta\theta} \frac{\partial^2 f}{\partial \theta_0^2} + g^{\zeta\zeta} \left( \frac{\partial}{\partial \zeta_0} - \frac{\partial}{q \partial \theta_0} \right)^2 f \\ &+ \frac{1}{J} \left( \frac{\partial J g^{\psi\psi}}{\partial \psi} + \frac{\partial J g^{\psi\theta}}{\partial \theta_0} \right) \frac{\partial f}{\partial \psi} + \frac{1}{J} \left( \frac{\partial J g^{\psi\theta}}{\partial \psi} + \frac{\partial J g^{\theta\theta}}{\partial \theta_0} \right) \frac{\partial f}{\partial \theta_0}. \end{aligned} \quad (31)$$

Using the fact the perpendicular scale length is much shorter than the parallel scalar length, the perpendicular Laplacian can be obtained from the preceding equation:

$$\begin{aligned} \nabla_{\perp}^2 f &= g^{\psi\psi} \frac{\partial^2 f}{\partial \psi^2} + 2g^{\psi\theta} \frac{\partial^2 f}{\partial \psi \partial \theta_0} + \left( g^{\theta\theta} + g^{\zeta\zeta} / q^2 \right) \frac{\partial^2 f}{\partial \theta_0^2} \\ &+ \frac{1}{J} \left( \frac{\partial J g^{\psi\psi}}{\partial \psi} + \frac{\partial J g^{\psi\theta}}{\partial \theta_0} \right) \frac{\partial f}{\partial \psi} + \frac{1}{J} \left( \frac{\partial J g^{\psi\theta}}{\partial \psi} + \frac{\partial J g^{\theta\theta}}{\partial \theta_0} \right) \frac{\partial f}{\partial \theta_0} \end{aligned} \quad (32)$$

Next we study how to discretize the preceding perpendicular Laplacian. In the GTC code, we use an unstructured mesh to ensure the roughly equal grid size in the radial and poloidal direction. The mesh grids are uniform in the  $\theta_0$  direction for each flux surface and non-uniform in the  $\psi$  direction. In order to evaluate the Laplacian numerically in Eq. (32), we need to discretize the following five operators:

$$\frac{\partial}{\partial \theta_0}, \frac{\partial}{\partial \psi}, \frac{\partial^2}{\partial \psi^2}, \frac{\partial^2}{\partial \psi \partial \theta_0} \text{ and } \frac{\partial^2}{\partial \theta_0^2}.$$

The discretization of these differential operators by the finite difference method is shown in Appendix II.

After discretizing each term in Eq. (32), we can convert the Poisson equation  $\nabla_{\perp}^2 \phi = \delta n(\psi, \theta)$  to a big-size matrix equation and solve it parallelly by using the software of PETSc [34]. A numeric example is provided to verify the numerical Poisson solver. In the simple circular cross section limit, we assume the safety factor  $q = \text{const}$ , then  $g^{\psi\psi} = r^2/q^2$ ,  $g^{\theta\theta} = 1/r^2$ ,  $g^{\psi\theta} = 0$ ,  $g^{\zeta\zeta} = 1/X^2$ , with  $X = 1 + r \cos \theta / R_0$ . Then the Laplace operator including the essential toroidal effect becomes

$$\nabla_{\perp}^2 = \frac{\partial^2}{\partial r^2} + \left( \frac{1}{r} + \frac{\cos \theta}{X} \right) \frac{\partial}{\partial r} + \left( \frac{1}{r^2} + \frac{1}{q^2 X^2} \right) \frac{\partial^2}{\partial \theta^2} - \frac{\sin \theta}{Xr} \frac{\partial}{\partial \theta}.$$

The source term in the Poisson equation is set as  $\delta n(r, \theta) = \nabla_{\perp}^2 \left[ \sin \left( 4\pi \frac{r - a_0}{a_1 - a_0} \right) \cos(m\theta) \right]$ , with  $m = 6$ , which is shown in Fig. 6(a) in the 2D

poloidal plane. Using the boundary condition  $\phi(r = a_0) = \phi(r = a_1) = 0$  and the new Poisson solver implemented in GTC, we can find the numeric solution to the Poisson equation, as shown in Fig. 6(b).

Then we find the numeric values along the black solid line in Fig. 6(b), and compare them to those from the analytic solution. As shown in Fig. 6(c), the numeric solution almost overlaps

the analytic solution, which verifies the effectiveness of this finite difference based Poisson solver.

## ***VI. Simulation for DIII-D Experiment***

Next we put together all the preceding newly developed features in GTC to simulate a real tokamak experiment based on the DIII-D discharge #101391[25]. This low  $\beta$  L-mode discharge has been carefully studied by the GYRO code [24]. Therefore, the simulation of this particular discharge will provide a useful benchmark case for the verification between the gyrokinetic codes through completely different approaches. In order to carry out a meaningful verification/validation, it is critical to compare the convention used in these codes. We first compare the convention of the input physical quantities in GTC with that in GYRO in the Appendix III. Then we use the GTC code to carry out an electrostatic turbulence simulation with kinetic electrons. The temperature and density profiles for ions and electrons are taken from the EFIT-produced iterdb file. Fig. 9 show the input profiles for the GTC simulation, with the simulation domain  $r \in [0.12a, 0.82a]$ . Since the zero boundary condition is assumed in the GTC simulation, we artificially flatten the plasma profiles in the two edges of the simulation domain to lower the turbulence drive in those regions.

In the PIC simulation, generally a limited number of particles are used to simulate a physical system with much larger number of particles. These particles in the simulation are called “markers”. For the background marker loading at the beginning of the simulation, we apply two different methods, namely the uniform loading and nonuniform loading. For the uniform loading method, the marker temperature and density are set to be uniform along the radial direction, which is equal to the value at the reference point  $r = r_{ref}$ , while still keeping the experimental temperature and density gradient profiles, as sketched by Fig. 10(a)(b). For the nonuniform loading method, we choose the marker temperature and density to faithfully follow the input profiles and their gradients, as shown by Fig. 10 (c)(d). The GTC code conventionally uses the uniform loading method since it has less Monte Carlo noise than nonuniform loading method for the same total number of particles in the simulation. As discussed in the preceding sections, the gyrokinetic Poisson equation can also be solved in two approaches, the improved 4-point average method or the Pade approximation method.

We show the time history of the volume averaged ion heat diffusivity in Fig. 11, with the red solid line denoting the uniform loading, the red circle line denoting the non-uniform loading. In these two cases the improved 4-point average method is used to solve the gyrokinetic Poisson equation. The blue square line in Fig. 11 shows the time history of the ion heat diffusivity for the non-uniform loading using the Pade approximation to solve gyrokinetic Poisson equation. All these three methods give the same level of turbulent transport, which indicates that the uniform loading method retain a good

approximation for the essential turbulent transport physics. In the mean while, it confirms the Pade approximation is as good as the 4-point average method to solve the gyrokinetic Poisson equation in the turbulence simulation.

Then we focus on the gyrokinetic simulation using nonuniform marker loading and the improved 4-point Poisson solver. The 3D global turbulence mode structure is displayed for the linear stage and nonlinear stage in Fig. 12 (a) and (b) respectively. In the linear stage, strong eigenmode structure forms along the radial direction. In the nonlinear stage, due to the excitation of the zonal flow, the predominant linear radial structure is totally destroyed. This confirms that the zonal flow plays an important role in regulating turbulence for this particular case.

The ion heat diffusivity is time-averaged during the nonlinear stage at each radial location, which gives the radial profile of the time averaged ion heat diffusivity, as shown by the red solid line in Fig. 13. As a comparison, the ion heat diffusivity profile from the GYRO simulation is also shown by the dashed line in Fig. 13. These two curves overlap each other very well, which provides a good verification example in the microturbulence simulation between two different gyrokinetic codes.

The results are then shown for the simulation which uses the Pade approximation to solve the gyrokinetic Poisson equation. The radial profiles of the time averaged ion and electron heat diffusivity are shown by the dashed lines in Fig. 14. In this Figure, the time averaged ion and electron heat diffusivity from the improved 4-point average method are also shown by the solid lines. These two different methods for the gyrokinetic equation give approximately similar radial profiles for the ion and electron heat diffusivity.

Next we compare the radial profiles for the time averaged ion heat diffusivity for the two marker loading method mentioned before. As shown by Fig. 15, the solid line is for the non-uniform loading and the dashed line is for the uniform loading. One can see that the ion heat diffusivity from the uniform loading is larger on the inner side than that from the non-uniform loading. On the outer side of the radius, the ion heat diffusivity for the uniform loading is smaller instead. This phenomenon can be explained by the fact that on the inner side of the radius, the marker temperature for the nonuniform loading is larger than that for the uniform loading, so is the ion gyroradius. Due to stabilizing effect of gyroaverage, i.e., the finite Larmor radius (FLR) effect, the linear growth rate for the nonuniform loading is smaller than that for the uniform loading on the inner side of the radius. So is the turbulence transport. The same argument can be applied to explain why on the outer side the turbulent transport for the uniform loading is smaller than that for the nonuniform loading.

## ***VII. Summary and discussion***

In this paper, we extend the GTC code to import experimental profiles and magnetic geometry and simulate turbulent transport in general geometry by using B-splines to interpolate the equilibrium data. A new Poisson solver based on flux coordinates and finite difference scheme is designed and successfully implemented in GTC, which can be used along with Pade approximation to solve the gyrokinetic Poisson equation. This new Poisson solver can be further used for electromagnetic simulations. We also improved the conventional 4-point average method to include higher order global effects for gyrokinetic Poisson equation. An electrostatic turbulence simulation is carried out for DIII-D discharge #101391 using the preceding two different approaches for the gyrokinetic Poisson solver. The resultant turbulent transport levels are found to be consistent with each other. The radial profile of the heat diffusivity is compared to that from GYRO and good agreement is found. For the background marder loading, we developed and tested a non-uniform loading method and found only small difference from the conventional uniform loading method on the volume averaged turbulent transport. But on the radial structure, there is a nontrivial difference between different loading methods. This difference is found due to the stabilizing effect of the gyroaverage (FLR effect). The new algorithm to solve Poisson equation using the flux coordinates can be used for electromagnetic simulation, where the Ampere's law has a similar Laplacian form. Another advantage of this new gyrokinetic Poisson solver is that it can be used to simulate the small aspect ratio tokamaks since the gyrokinetic Poisson equation is solved in the perpendicular plane other than poloidal plane in the conventional GTC simulation.

## ***Acknowledgments***

The work is supported by the National Magnetic Confinement Fusion Science Program under Grant No. 2011GB105001 and 2013GB111000, China NSFC under Grant No. 91130031, the Recruitment Program of Global Youth Experts, US DOE SciDac GSEP centers. One of the authors, Y. Xiao, thanks R. Waltz for providing DIII-D data and C. Holland for useful discussions .

## ***Appendix I: B-spline interpolation***

For 1D function  $f(\psi)$  define at the points  $\psi_i$ , we can use B-spline to find its value at any space points,  $f(\psi) = f(1,i) + f(2,i)h + f(3,i)h^2$ , with  $h = \psi_{i+1} - \psi_i$ ,  $i = 0, 1, \dots, N$ . Here the function values at the grid point  $\psi_i$  is known, i.e.,  $f(1,i)$ . We try to find the other B-spline coefficients,  $f(2,i)$

and  $f(3,i)$ , by using the known values  $f(1,i)$ . By using zeroth and first order continuous condition one dimensional function  $f(\psi)$  or two dimensional function  $f(\psi,\theta)$ . For the 1D function  $f(\psi)$ , such as ion temperature profile  $T_i(\psi)$  and toroidal current  $g(\psi)$ , we use the following B-spline representation

$$f(\psi) = f(1,i) + f(2,i)h + f(3,i)h^2, \quad (33)$$

where  $\psi_i \leq \psi < \psi_{i+1}$ ,  $h = \psi_{i+1} - \psi_i$ ,  $i = 0, 1, \dots, N$ .

$$f(x_i + h) = f(x_{i+1}), f'(x_i + h) = f'(x_{i+1}), \quad (34)$$

We find that

$$f(1,i+1) = f(1,i) + f(2,i)h + f(3,i)h^2, \quad (35)$$

$$f(2,i+1) = f(2,i) + 2f(3,i)h. \quad (36)$$

The preceding two iterative equations are used to obtain the B-spline coefficients,  $f(2,i)$  and  $f(3,i)$ . However, the two initial values,  $f(2,1)$  and  $f(3,1)$  remain to be determined, which turns out to rely on the specific feature of the function  $f(\psi)$  around the initial point  $\psi_0$ . When  $\psi \rightarrow \psi_0$ , there are four relevant cases to be considered.

Case 1:  $f(\psi) = a + b\Delta\psi$ , where  $\Delta\psi \equiv \psi - \psi_0$ . In this case, the coefficients  $f(2,1)$  and  $f(3,1)$  are found to be

$$f(2,1) = [f(1,2) - f(1,1)]/h \quad (37)$$

$$f(3,1) = 0 \quad (38)$$

Case 2:  $f(\psi) = a + b\Delta\psi^2$ , in which the coefficients  $f(2,1)$  and  $f(3,1)$  are found to be

$$f(2,1) = 0 \quad (39)$$

$$f(3,1) = [f(1,2) - f(1,1)]/h^2 \quad (40)$$

Case 3:  $f(\psi) = a + b\Delta\psi + c\Delta\psi^2$ , in which the coefficients  $f(2,1)$  and  $f(3,1)$  are found to be

$$f(2,1) = [4f(1,2) - f(1,3) - 3f(1,1)] / (2h) \quad (41)$$

$$f(3,1) = [f(1,2) - f(1,1) - f(2,1)h] / h^2 \quad (42)$$

Case 4:  $f(x) = a + b\sqrt{\Delta\psi} + c\Delta\psi$ . This case needs special care to find a smooth  $f(1,i)$  and the iteration equations become

$$f(2,i) = -f(2,i-1) + 2[f(1,i) - f(1,i-1)] / h \quad (43)$$

$$f(1,i+1) = f(2,i) / (2h) + f(1,i+2) / 4 + 3f(1,i) / 4 \quad (44)$$

$$f(3,i) = [f(2,i+1) - f(2,i)] / 2h \quad (45)$$

In order to evolve the preceding equations, the initial coefficients  $f(2,1)$  and  $f(3,1)$  are found to be

$$f(2,1) = [2f(1,2) - f(1,3) - f(1,1)] / [(2 - \sqrt{2})\sqrt{h}] \quad (46)$$

$$f(3,1) = [f(1,2) - f(1,1) - f(2,1)\sqrt{h}] / h \quad (47)$$

and the initial coefficients  $f(2,2)$  and  $f(3,2)$  are found to be

$$f(2,2) = f(3,1) + f(2,1) / (2\sqrt{h}) \quad (48)$$

$$f(3,2) = [f(1,3) - f(1,2) - hf(2,2)] / h^2 \quad (49)$$

The end point needs also special treatment:

$$f(2,N-1) = -f(2,N-2) + 2[f(1,N-1) - f(1,N-2)] / h \quad (50)$$

We note that with the above settings, the inversion of these B-spline functions can be obtained.

## Appendix II: Discretization of differential operator on the GTC unstructured mesh

Since the grid size in the  $\theta_0$  is uniform for each flux surface, we can apply a simple spatial central algorithm to discretize  $\frac{\partial}{\partial \theta_0}$  to the second order accuracy.

$$\left( \frac{\partial f}{\partial \theta_0} \right)_{i,j} = \frac{f_{i,j+1} - f_{i,j-1}}{2(\Delta \theta_0)_i}, \quad (51)$$

where  $i$  is the index label for  $\psi$ ,  $j$  is the index label for  $\theta_0$ , as shown in Fig. 5.

Then we discretize  $\frac{\partial}{\partial \psi}$  to obtain

$$\left( \frac{\partial f}{\partial \psi} \right)_{i,j} = w_2 \frac{f_{i+1,j^*} - f_{i,j}}{h_2} + w_1 \frac{f_{i,j} - f_{i-1,j^*}}{h_1}, \quad (52)$$

with  $h_1 = \psi_i - \psi_{i-1}$ ,  $h_2 = \psi_{i+1} - \psi_i$ , and  $w_2 = h_1/(h_1 + h_2)$ ,  $w_1 = h_2/(h_1 + h_2)$ . The value of  $f_{i+1,j^*}$  can be evaluated using the neighboring four points on the same flux surface  $\psi_{i+1}$ , as shown in Fig. 5, to the second order of accuracy:

$$\begin{aligned} f_{i+1,j^*} = & w_{i+1} f_{i+1,j'+1} + \lambda_{i+1} f_{i+1,j'} + \frac{\lambda_{i+1} w_{i+1}}{2} [w_{i+1} f_{i+1,j'+1} + \\ & \lambda_{i+1} f_{i+1,j'} - \frac{1}{3}(1 + w_{i+1}) f_{i+1,j'+2} - \frac{1}{3}(1 + \lambda_{i+1}) f_{i+1,j'-1}] \end{aligned} \quad (53)$$

where  $w_{i+1} = (\theta - \theta_{i+1,j'}) / \Delta \theta_{i+1}$ , and  $\lambda_{i+1} = 1 - w_{i+1}$ . A similar expression can be found for the value  $f_{i-1,j^*}$ .

We continue to discretize  $\frac{\partial^2}{\partial \theta_0 \partial \psi}$  to obtain

$$\left( \frac{\partial^2 f}{\partial \theta_0 \partial \psi} \right)_{i,j} = \left( \frac{w_1}{h_1} - \frac{w_2}{h_2} \right) \frac{f_{i,j+1} - f_{i,j-1}}{2\Delta \theta_i} + \frac{w_2}{h_2} \frac{\partial f_{i+1,j^*}}{\partial \theta_0} - \frac{w_1}{h_1} \frac{\partial f_{i-1,j^*}}{\partial \theta_0} \quad (54)$$

Using the four neighboring points in the same flux surface, we can obtain

$$\frac{\partial f_{i+1,j^*}}{\partial \theta_0} = \frac{1}{2\Delta\theta_{i+1}} [\lambda_{i+1}(f_{i+1,j'+1} - f_{i+1,j'-1}) + w_{i+1}(f_{i+1,j'+2} - f_{i+1,j'}) + \frac{1}{3}(1 - 3\lambda_{i+1}w_{i+1})(f_{i+1,j'-1} - 3f_{i+1,j'} + 3f_{i+1,j'+1} - f_{i+1,j'+2})] \quad (55)$$

Similar expressions can be written for  $\frac{\partial f_{i-1,j^*}}{\partial \theta_0}$ . Finally we deal with the operator  $\frac{\partial^2}{\partial \psi^2}$ .

$$\left( \frac{\partial^2 f}{\partial \psi^2} \right)_{i,j} = \frac{2}{h_1 h_2} (w_1 f_{i-1,j^*} + w_2 f_{i+1,j^*} - f_{i,j}) \quad (56)$$

where  $f_{i+1,j^*}$  can be evaluated by the four point interpolation using Eq. (53). Similar expression can be found for  $f_{i-1,j^*}$ .

### **Appendix III: Convention issues for GTC and GYRO**

The DIII-D discharge #101391 serves as a concrete example to discuss the difference between these two codes. The GTC code can create an analytic equilibrium based on circular cross section model or input a numerical equilibrium from the EFIT data, with the latter usually used to precisely compare to experiments. All figures about the DIII-D shot #101391 in this paper are taken from the GTC's output data, and then translated to GYRO convention if necessary. As shown in Fig. 8, each flux surface represents a particular value of the poloidal flux function  $\psi = \psi(R, Z)$ . The center of each flux surface  $\psi$  has the coordinate  $(R_0, Z_0)$ , where  $Z_0 \equiv \oint dZRZ / \oint dZR$ , and  $R_0 \equiv (R_+ - R_-) / 2$ , with  $R_-$  and  $R_+$  the intersection points of the flux surface and the horizontal line  $Z = Z_0$ . As shown by Fig. 8(a), the levitation of the flux surface center  $Z_0$  is negligibly small for all flux surfaces. Starting from the flux surface center, we can define a set of new coordinates  $(r, \theta)$ , as shown by Fig. 7, which leads to  $R_+ = R_0 + r(\psi, \theta = 0)$ ,  $R_- = R_0 - r(\psi, \theta = \pi)$ . Then on the flux surface  $\psi$ , the effective radius in the GTC code is set as  $r \equiv r(\psi, \theta = 0) = R_+ - R_0$ , which becomes a flux surface function. In the GYRO code, the effective radius  $r_g$  defined slightly differently,  $r_g \equiv [r(\psi, \theta = 0) + r(\psi, \theta = \pi)] / 2 = (R_+ - R_-) / 2$ . The effective radius  $r_{gic}$  and  $r_{gyro}$  are shown in Fig. 8(c) to vary with the poloidal flux  $\psi$ . Another useful effective radial variable  $\rho = \rho(\psi)$  is also

used in the GYRO code, with the definition  $\psi_T = B_0 \rho^2 / 2$  and  $B_0$  is the magnetic field at the magnetic axis. The toroidal magnetic flux  $\psi_T$  is related the poloidal magnetic flux  $\psi$  by the following relation  $d\psi_T/d\psi = q(\psi)$ , where  $q$  is the safety factor. The quantity,  $\rho d\rho/(r_g dr_g)$ , as shown by Fig. 8(d) for DIII-D discharge #101391., is important for determining the local effective magnetic field at the reference point,  $B_{unit} = B_0 \frac{\rho d\rho}{r_g dr_g}$ . In the GYRO convention, the normalized gyroradius  $\rho_* = \rho_s/a$ , where  $\rho_s = c_s/\Omega_i$ , and  $c_s = \sqrt{T_e/m_i}$ ,  $\Omega_i = \frac{q_i B_{unit}}{cm_i}$ . For the case DIII-D discharge #101391,  $R_0(0)=1.72m$ . According to Fig. 8 and 10, at the reference point  $r_{gyro}/a=0.60$ ,  $R_0 = 0.98R_0(0)=1.69m$ . In Fig. 8, we see that  $a=0.362R_0(0)=0.62m$ . We can obtain  $T_e=1.28kev$  at the reference point  $r_g/a=0.60$  from Fig. 9(a). Since in this discharge,  $B_0 = 2.106T$ , then at the reference point  $B_{unit} = 3.085T$ . These parameters give  $\rho_s = 0.0017m$  and then  $\rho_s/a=0.0027$ . This value is the same as the Ref. [25]. In order to make better comparison, we list some key parameters in Table (I) for GTC and GYRO [24, 25] for DIII-D discharge #101391. As shown by Table (I), the GTC parameters are very close to that of GYRO with some error within a few percentage.

	GTC	GYRO
$a$ (m)	0.62	0.63
$R_0$ (m)	1.69	1.69
$B_0$ (T)	2.11	2.1
$\rho_*$	0.0027	0.0026
$q$	1.55	1.59
$T_e$ (kev)	1.28	1.25
$\chi_{GB}$ ( $m^2/sec$ )	1.14	1.02

Table I: Some important equilibrium parameters at  $r/a=0.6$  for DIII-D discharge #101391. The GYRO parameters are taken from Ref.[24, 25].

The definition of heat diffusivity is another issue. The GTC code employs the heat flux  $\bar{q}$  to compute heat diffusivity  $\chi_{gic}^{ITER}$ , with

$$\bar{q} = \int d^3v \delta\bar{v}_E \delta f \left( \frac{mv^2}{2} - \frac{3}{2}T \right) \quad (57)$$

$$\chi_{gic}^{ITER} = \frac{\langle \bar{q} \cdot \nabla \psi \rangle}{n \langle |\nabla \psi|^2 \rangle \frac{\partial T}{\partial \psi}} \quad (58)$$

Where the  $\langle \rangle$  refers to the flux surface average. However, The GYRO code employs the heat flux  $\bar{Q}$  to compute heat diffusivity  $\chi_{gyro}^{ITER}$ ,

$$\bar{Q} = \int d^3v \delta\bar{v}_E \delta f \frac{mv^2}{2} \quad (59)$$

$$\chi_{gyro}^{ITER} = \frac{\langle \bar{Q} \cdot \nabla \psi \rangle}{n \langle |\nabla \psi|^2 \rangle \frac{\partial T}{\partial \psi}} \quad (60)$$

In principle, the symbol  $\psi$  in Eq. (57) and (59) could be any flux surface function, such as  $r_{gic}$ ,  $r_{gyro}$  or  $\rho$ . In the ITER definition, the symbol  $\psi$  refers specifically to the poloidal magnetic flux. The relationship between  $\chi_{gic}^{ITER}$  and  $\chi_{gyro}^{ITER}$  can be described the following equation,

$$\chi_{gyro}^{ITER} = \chi_{gic}^{ITER} + \frac{3}{2} \frac{T \partial n / \partial \psi}{n \partial T / \partial \psi} \frac{\langle \bar{\Gamma} \cdot \nabla \psi \rangle}{\langle |\nabla \psi|^2 \rangle \partial n / \partial \psi} \quad (61)$$

Where the particle flux is defined as

$$\bar{\Gamma} = \int d^3v \delta\bar{v}_E \delta f \quad (62)$$

## References

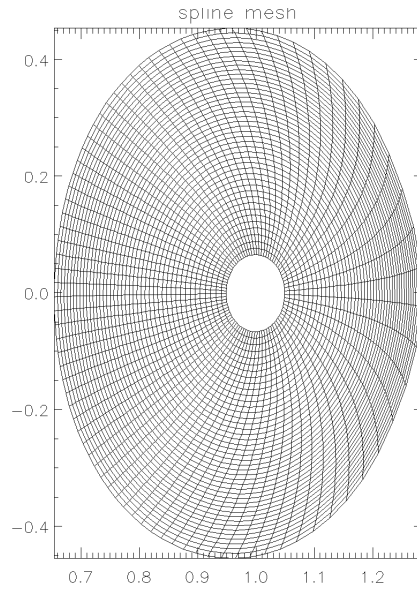
1. Doyle, E.J., et al., *Chapter 2: Plasma confinement and transport*. Nuclear Fusion, 2007. **47**(6): p. S18-S127.

2. Horton, W., *Drift waves and transport*. Reviews of Modern Physics, 1999. **71**(3): p. 735-778.
3. Li, J.Q. and Y. Kishimoto, *Gyrofluid Simulation of Ion-Scale Turbulence in Tokamak Plasmas*. Communications in Computational Physics, 2008. **4**(5): p. 1245-1257.
4. Ross, D.W., W.M. Tang, and J.C. Adam, *STUDY OF TRAPPED ELECTRON INSTABILITIES DRIVEN BY MAGNETIC CURVATURE DRIFTS*. Physics of Fluids, 1977. **20**(4): p. 613-618.
5. Lin, Z., et al., *Turbulent transport reduction by zonal flows: Massively parallel simulations*. Science, 1998. **281**(5384): p. 1835-1837.
6. Dimits, A.M., et al., *Parameter dependences of ion thermal transport due to toroidal ITG turbulence*. Nuclear Fusion, 2001. **41**(11): p. 1725-1732.
7. Xiao, Y., P.J. Catto, and W. Dorland, *Effects of finite poloidal gyroradius, shaping, and collisions on the zonal flow residual*. Physics of Plasmas, 2007. **14**(5).
8. Lin, Z., et al., *Size scaling of turbulent transport in magnetically confined plasmas*. Physical Review Letters, 2002. **88**(19).
9. Xiao, Y. and Z. Lin, *Convective motion in collisionless trapped electron mode turbulence*. Physics of Plasmas, 2011. **18**(11).
10. Holland, C., et al., *Implementation and application of two synthetic diagnostics for validating simulations of core tokamak turbulence*. Physics of Plasmas, 2009. **16**(5).
11. Rhodes, T.L., et al., *L-mode validation studies of gyrokinetic turbulence simulations via multiscale and multifield turbulence measurements on the DIII-D tokamak*. Nuclear Fusion, 2011. **51**(6).
12. Holland, C., et al., *Advances in validating gyrokinetic turbulence models against L- and H-mode plasmas*. Physics of Plasmas, 2011. **18**(5).
13. Holod, I., et al., *Electromagnetic formulation of global gyrokinetic particle simulation in toroidal geometry*. Physics of Plasmas, 2009. **16**(12).
14. Spong, D.A., et al., *Verification and validation of linear gyrokinetic simulation of Alfvén eigenmodes in the DIII-D tokamak*. Physics of Plasmas, 2012. **19**(8).
15. Wang, Z., et al., *Radial Localization of Toroidicity-Induced Alfvén Eigenmodes*. Physical Review Letters, 2013. **111**(14).
16. Fulton, D.P., et al., *Microturbulence in DIII-D tokamak pedestal. I. Electrostatic instabilities*. Physics of Plasmas, 2014. **21**(4).
17. McClenaghan, J. and Z. Lin, in preparation for Phys of Plasmas, 2014.
18. Bao, J., et al., *Particle simulation of lower hybrid wave propagation in fusion plasmas*. 2014: *Plasma Phys. Contr. Fusion* p. 95020.
19. Ren, Q., et al., *High spatial resolution equilibrium reconstruction*. Plasma Physics and Controlled Fusion, 2011. **53**(9).
20. Lao, L.L., et al., *3-DIMENSIONAL TOROIDAL EQUILIBRIA AND STABILITY BY A VARIATIONAL SPECTRAL METHOD*. Physics of Fluids, 1985. **28**(3): p. 869-877.
21. Hirshman, S.P. and J.C. Whitson, *STEEPEST-DESCENT MOMENT METHOD FOR 3-DIMENSIONAL MAGNETOHYDRODYNAMIC EQUILIBRIA*. Physics of Fluids, 1983. **26**(12): p. 3553-3568.
22. Goldston, R.J., et al., *NEW TECHNIQUES FOR CALCULATING HEAT AND PARTICLE SOURCE RATES DUE TO NEUTRAL BEAM INJECTION IN AXISYMMETRIC TOKAMAKS*. Journal of Computational Physics, 1981. **43**(1): p. 61-78.
23. Lee, W.W., *GYROKINETIC PARTICLE SIMULATION-MODEL*. Journal of Computational Physics, 1987. **72**(1): p. 243-269.
24. Waltz, R.E., J. Candy, and M. Fahey, *Coupled ion temperature gradient and trapped electron mode to electron temperature gradient mode gyrokinetic simulations*. Physics of Plasmas, 2007. **14**(5).
25. Candy, J. and R.E. Waltz, *Anomalous transport scaling in the DIII-D tokamak matched by supercomputer simulation*. Physical Review Letters, 2003. **91**(4).
26. Hahm, T.S., *NONLINEAR GYROKINETIC EQUATIONS FOR TOKAMAK MICROTURBULENCE*. Physics of Fluids, 1988. **31**(9): p. 2670-2673.

27. Lin, Z., et al., *Global gyrokinetic particle simulations with kinetic electrons*. Plasma Physics and Controlled Fusion, 2007. **49**(12B): p. B163-B172.
28. Parker, S.E. and W.W. Lee, *A FULLY NONLINEAR CHARACTERISTIC METHOD FOR GYROKINETIC SIMULATION*. Physics of Fluids B-Plasma Physics, 1993. **5**(1): p. 77-86.
29. White, R.B. and M.S. Chance, *HAMILTONIAN GUIDING CENTER DRIFT ORBIT CALCULATION FOR PLASMAS OF ARBITRARY CROSS-SECTION*. Physics of Fluids, 1984. **27**(10): p. 2455-2467.
30. Lee, W.W., *GYROKINETIC APPROACH IN PARTICLE SIMULATION*. Physics of Fluids, 1983. **26**(2): p. 556-562.
31. Lewandowski, J.L.V., et al., *Global particle-in-cell simulations of microturbulence with kinetic electrons*. Physics of Plasmas, 2006. **13**(7).
32. Lin, Z. and W.W. Lee, *METHOD FOR SOLVING THE GYROKINETIC POISSON EQUATION IN GENERAL GEOMETRY*. Physical Review E, 1995. **52**(5): p. 5646-5652.
33. Zhang, H.S. and Z. Lin, *Trapped electron damping of geodesic acoustic mode*. Physics of Plasmas, 2010. **17**(7).
34. Balay, S., et al. *PETSc Web page*. 2014; Available from: <http://www.mcs.anl.gov/petsc>.

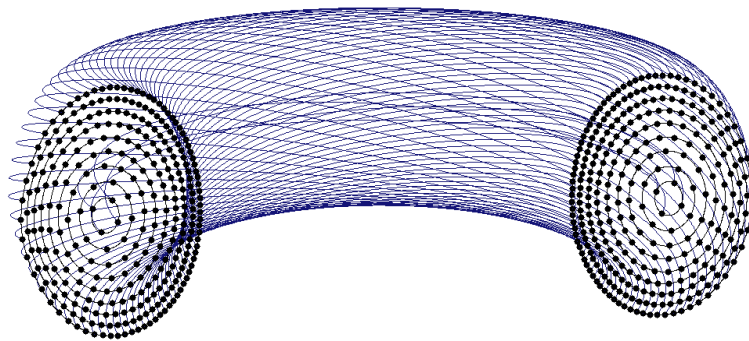
## Figure lists

Figure 1. Equilibrium mesh



**Fig 1.** Equilibrium mesh from EFIT data. The solid lines are drawn along constant  $\psi$  and  $\theta$ .

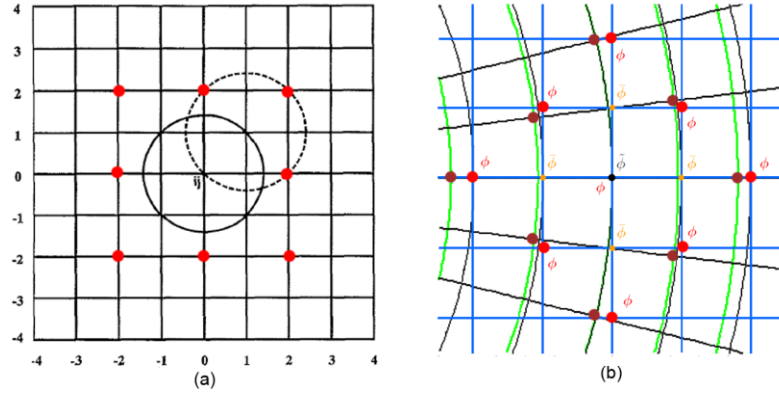
Figure 2. Unstructured mesh in GTC



**Fig 2.** Sketch of Unstructured field-aligned mesh in GTC. The grids are

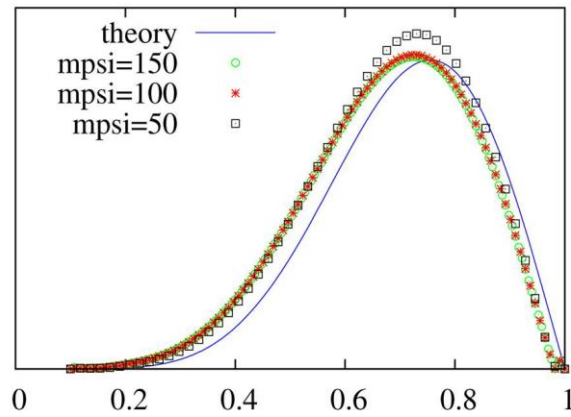
usually set to make the radial grid size and poloidal grid size equal.

Figure 3. Four-point average revisited



**Fig 3** (a) Eight extra points are required to compute  $\tilde{\phi}$  based on the four-point gyro-average method. (b) the points used to compute  $\tilde{\phi}$  in the current GTC (fresh red points) capture the global effect while the points used conventionally (dark red points) are based on the local approximation.

Figure 4. Verification of four-point average



(a)

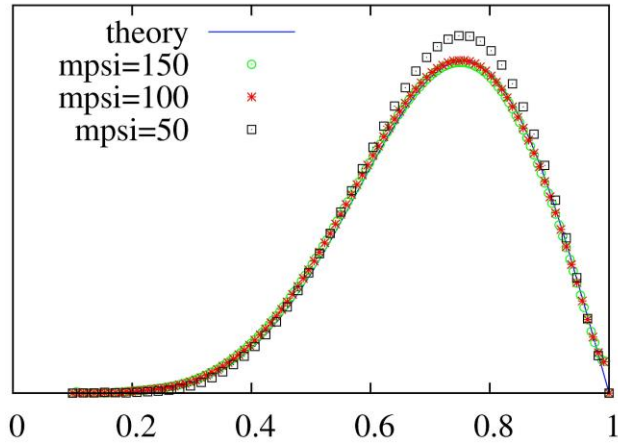
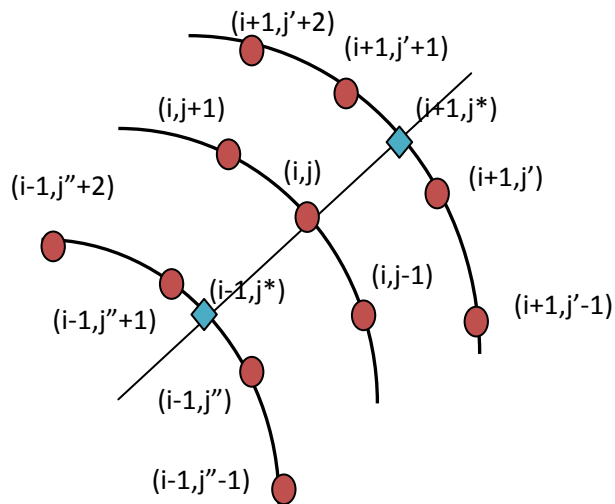


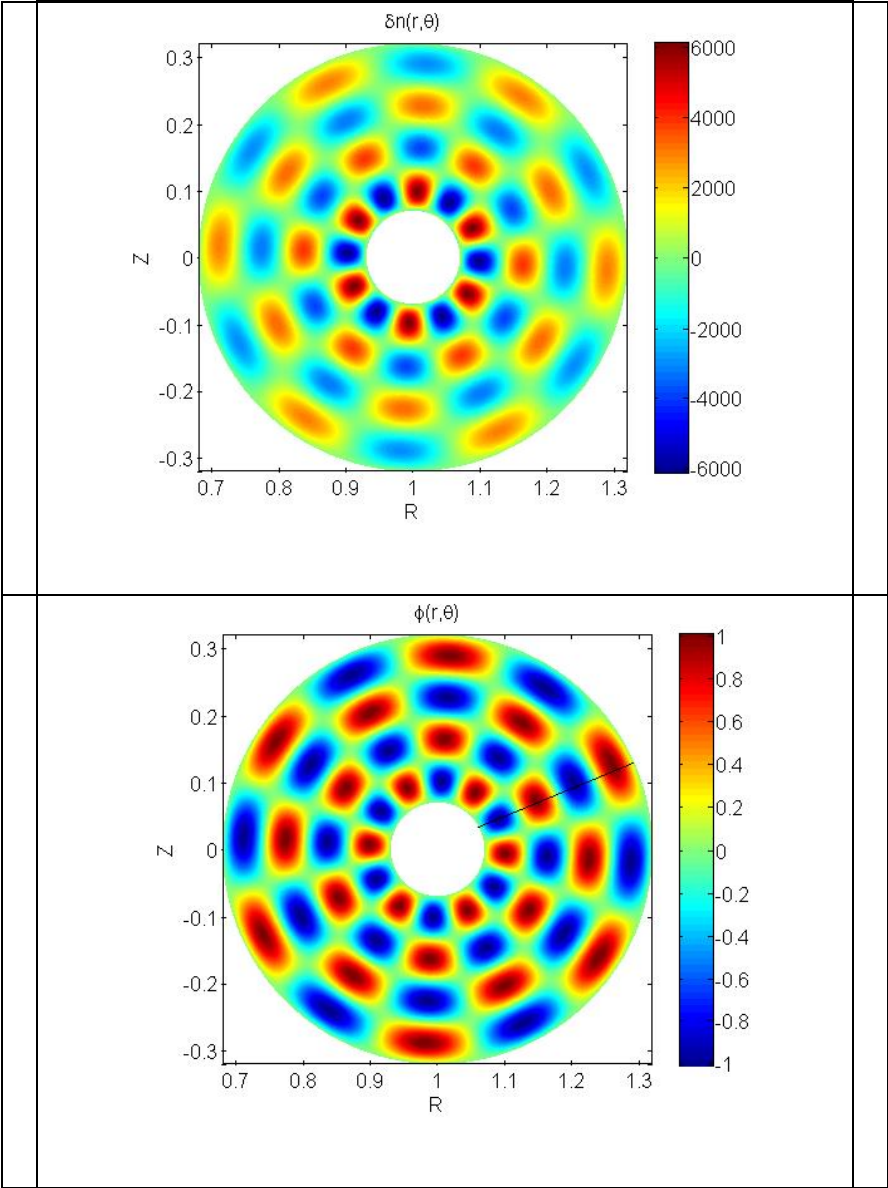
Fig 4. The four-point average applied to compute the  $\tilde{\phi}$  are verified in the Bessel problem, for the following two cases (a) with local approximation, (b) with global correction.

Figure 5. Laplacian discretizaion



**Fig 5.** Discretization of Laplacian at mesh point  $(i,j)$  involves additional 10 points around it.

Figure 6. Verification of Poisson solver



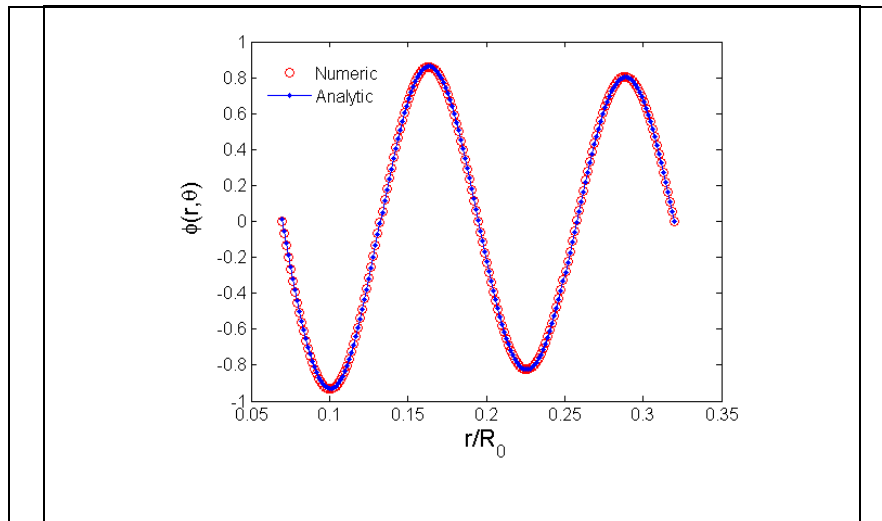


Fig 6 Verification of Poisson solver by a sample problem.

Figure 7 Equilibrium flux surface for DIII-D shot # 101391

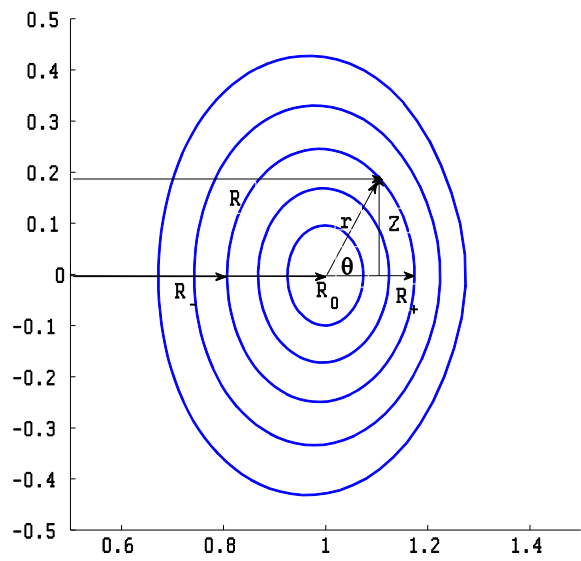
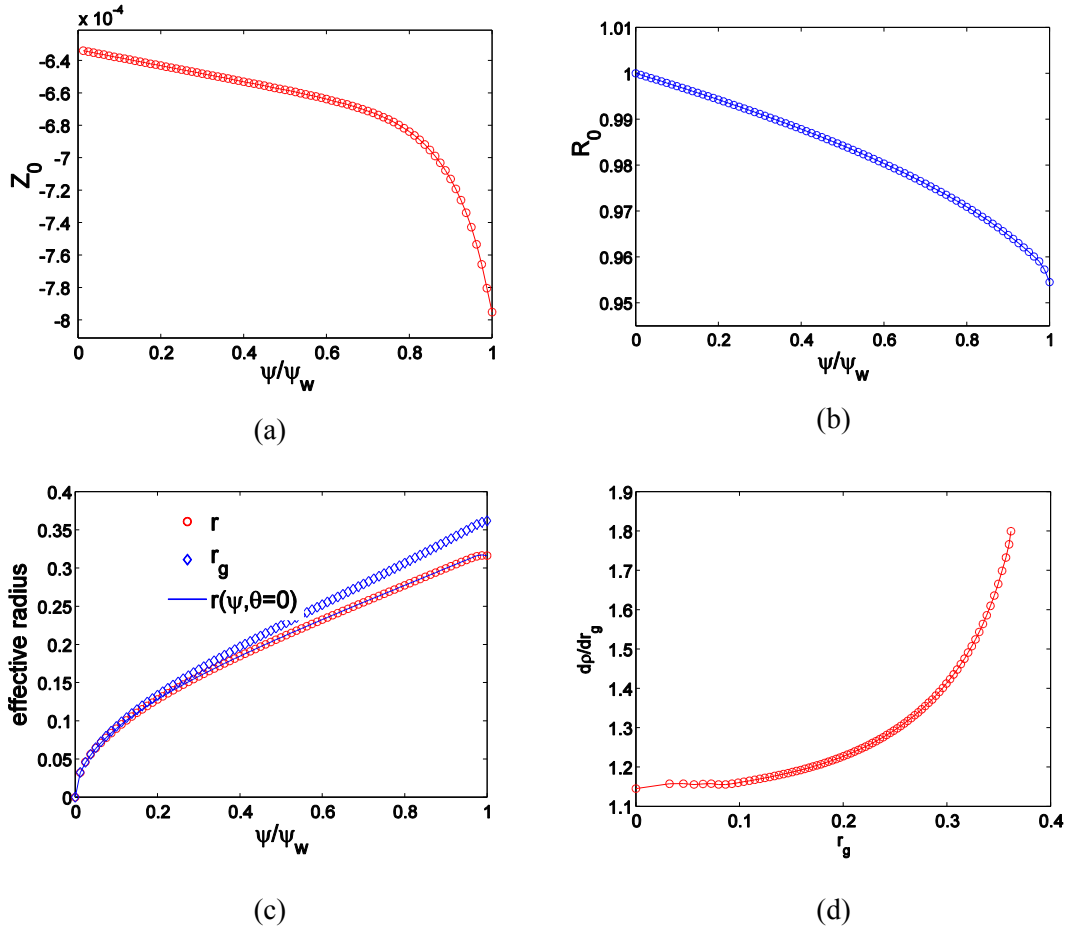


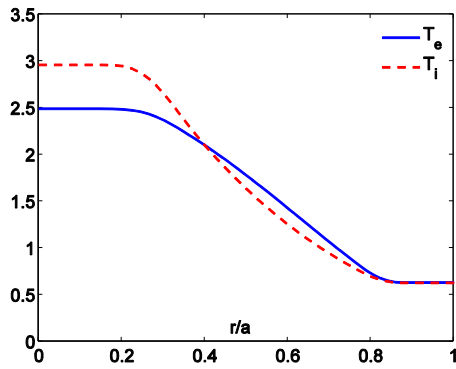
Fig 7: Equilibrium flux surface for DIII-D Shot #101391 are demonstrated to show the coordinate definition in GTC and GYRO.

Figure 8. Radial Coordinate Conventions

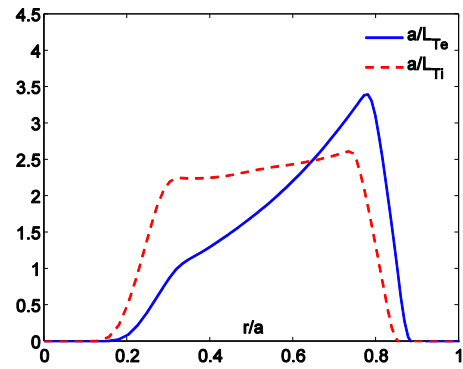


**Fig 8** In the case of DIII-D Shot #101391: (a)  $Z_0$  in unit of  $R_0(0)$  varies with poloidal flux surface  $\psi$ . (b)  $R_0$  in unit of  $R_0(0)$  varies with poloidal flux surface  $\psi$ . (c) Effective radius for GTC  $r$ , for GYRO  $r_g$  and  $r(\psi, \theta=0)$  in unit of  $R_0(0)$  varies with poloidal flux surface  $\psi$ . (d)  $\frac{d\rho}{dr_g}$  varies with  $r_g$  in unit of  $R_0(0)$ , which is used to calculate the effect magnetic field  $B_{unit}$ .

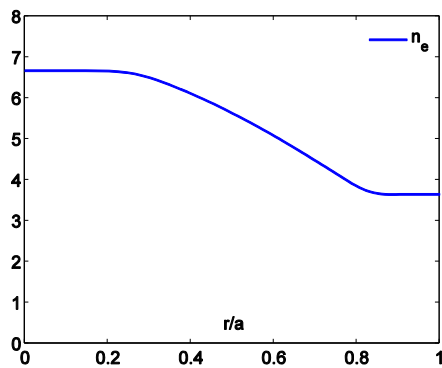
Figure 9. Radial profiles for DIII-D Shot #101391



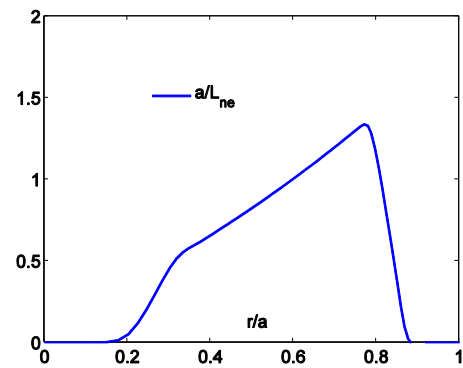
(a)



(b)



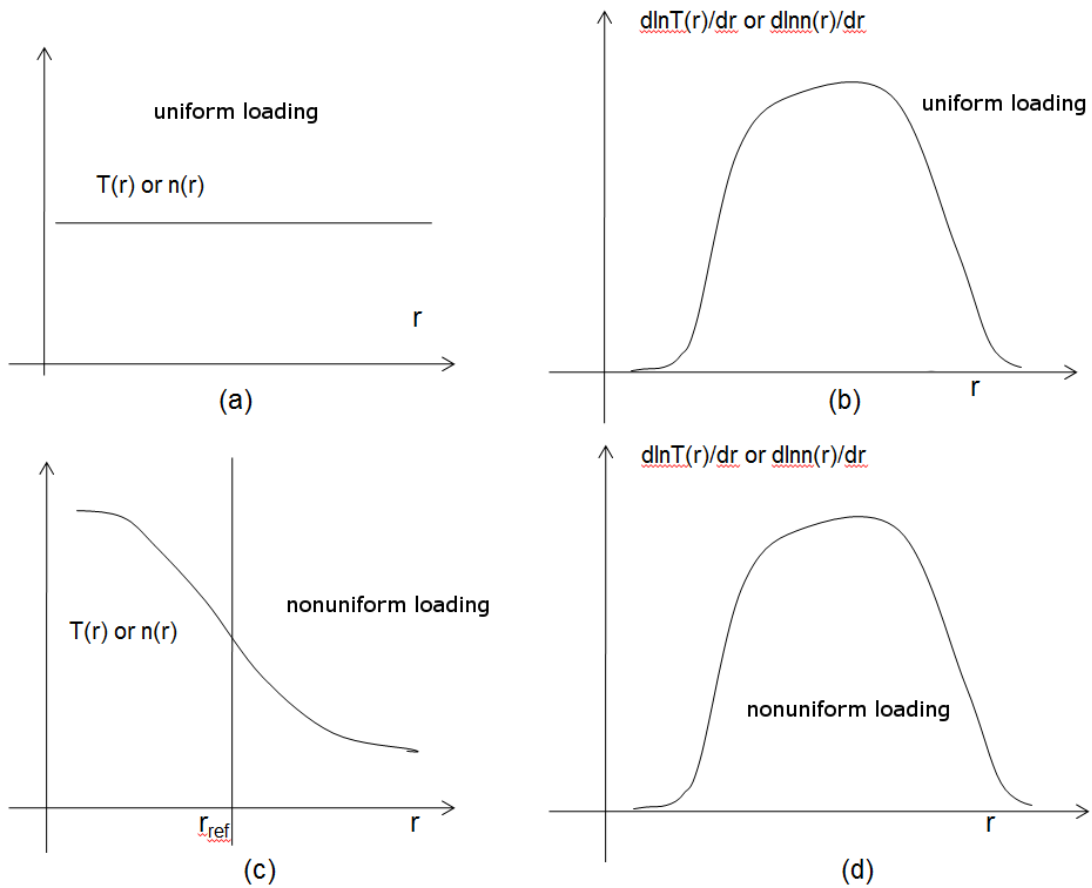
(c)



(d)

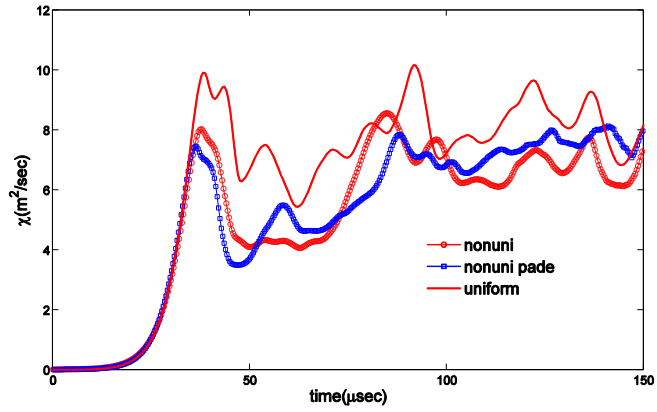
Fig 9. Radial profiles from GTC for the following equilibrium quantities: (a) electron and ion temperature, (b) electron and ion temperature gradient, (c) electron density (d) electron density gradient.

Figure 10 Background plasma profile setting



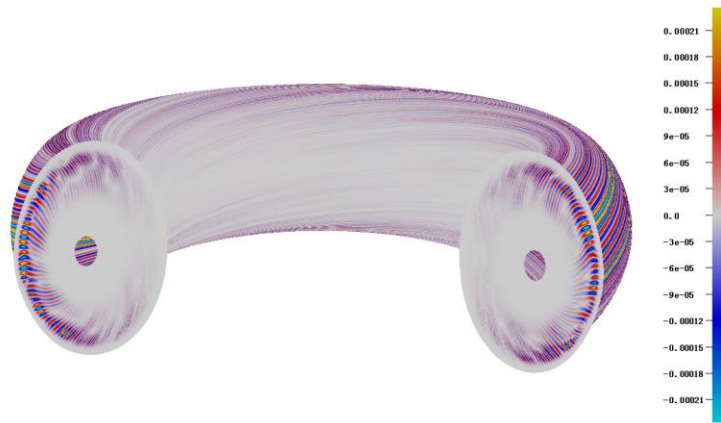
**Fig 10** Sketch of loading scheme of the background particle distribution in the GTC simulation: (a)(b) uniform loading: uniform radial profiles for marker temperature and density with real/non-uniform temperature and density gradients to excite instability; (c)(d) nonuniform loading real/non-uniform radial profiles for marker temperature and density with real/non-uniform temperature and density gradients to excite instability. For the uniform loading, the temperature/density in Fig. (a) is set as the value at the reference point  $r = r_{ref}$  in Fig. (c).

Figure 11 Time history of ion heat diffusivity



**Fig 11:** Time history of the ion heat diffusivity for three difference cases, where uniform means that that uniform marker loading with improved four-point average method to solve gyrokinetic Poisson equation, nonuni means that non-uniform marker loading with improved four-point average method, and nonuni pade means that non-uniform marker loading with Pade approximation to solve gyrokinetic Poisson equation.

Figure 12 Three-dimensional contour of turbulence structure



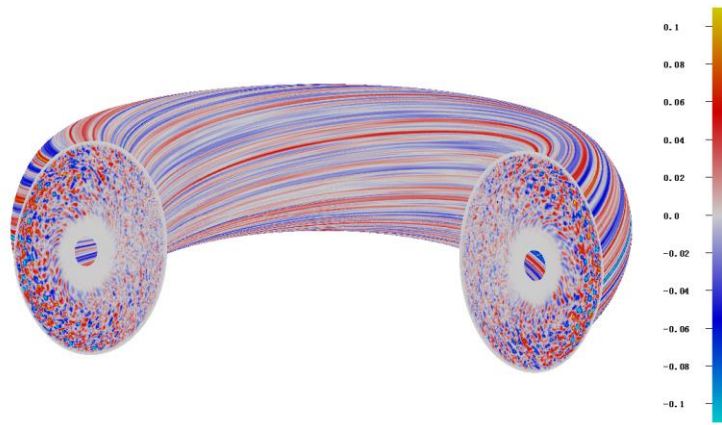


**Fig 12** Gyrokinetic simulation of DIII-D discharge #101391, global mode structure in the (a) linear growth stage (b) nonlinear stage.

Figure 13. Radial profile of ion heat diffusivity

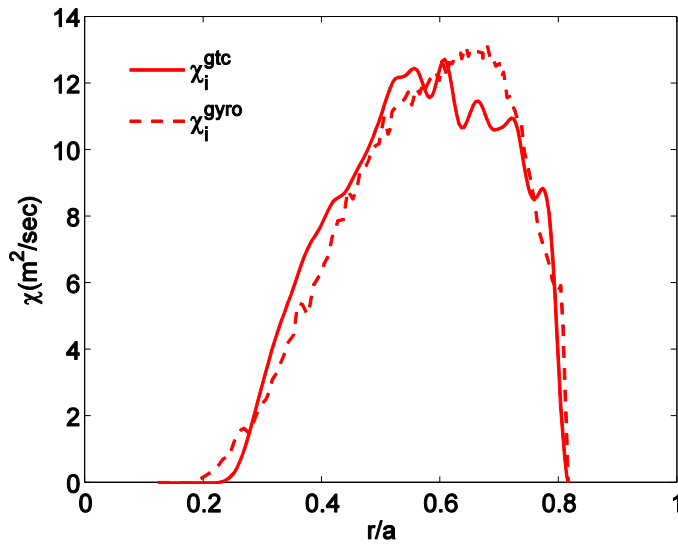


**Fig 13:** Comparison of radial profiles of ion heat diffusivity from GTC and GYRO simulation

Fig. 14 Heat diffusivity radial profiles from four-point-average method and Pade approximation

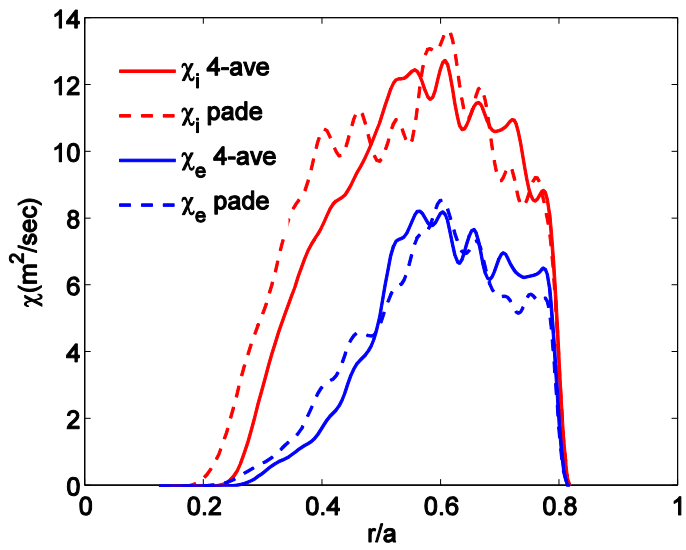


Fig 14: time averaged heat diffusivity radial profiles from four-point-average (4-ave) method and Pade approximation

Fig. 15 Heat diffusivity radial profiles for two marker loading methods

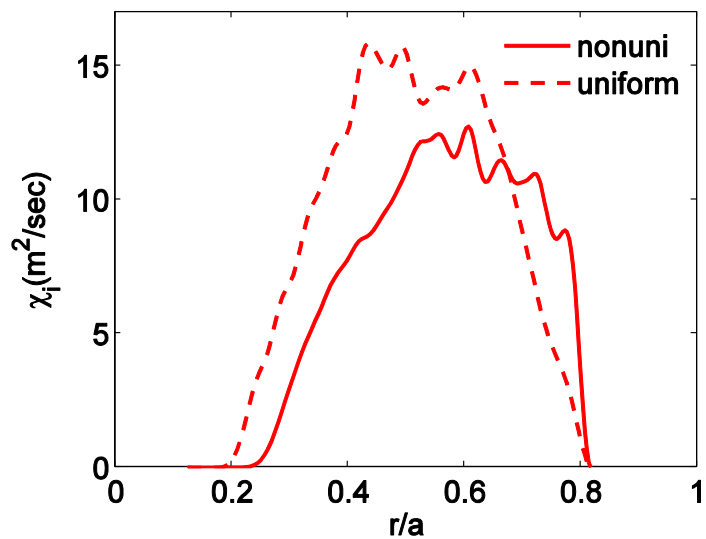


Fig 15: Heat diffusivity radial profile from two different marker loading methods, where uniform means the uniform marker loading and nonuni means the nonuniform marker loading.

